LAWRENCE
LIVERMORE
NATIONAL
LABORATORY

LLNL-JRNL-771023

Enhanced Tunability of Gold Nanoparticle Size, Spacing, and Shape for Large-Scale Plasmonic Arrays

N. J. Ray, J. H. Yoo, J. T. McKeown, S. Elhadj, S. H. Baxamusa, M. A. Johnson, H. T. Nguyen, W. Steele, J. M. Chesser, M. J. Matthews, E. Feigenbaum

April 2, 2019

Nano Letters

Disclaimer

This document was prepared as an account of work sponsored by an agency of the United States government. Neither the United States government nor Lawrence Livermore National Security, LLC, nor any of their employees makes any warranty, expressed or implied, or assumes any legal liability or responsibility for the accuracy, completeness, or usefulness of any information, apparatus, product, or process disclosed, or represents that its use would not infringe privately owned rights. Reference herein to any specific commercial product, process, or service by trade name, trademark, manufacturer, or otherwise does not necessarily constitute or imply its endorsement, recommendation, or favoring by the United States government or Lawrence Livermore National Security, LLC. The views and opinions of authors expressed herein do not necessarily state or reflect those of the United States government or Lawrence Livermore National Security, LLC, and shall not be used for advertising or product endorsement purposes.

Enhanced Tunability of Gold Nanoparticle Size, Spacing, and Shape for Large-Scale Plasmonic Arrays

*Nathan J. Ray; Jae H. Yoo; Joseph T. McKeown; Selim Elhadj; Salmaan H. Baxamusa; Michael A. Johnson; Hoang T. Nguyen; William A. Steele; John M. Chesser; Manyalibo J. Matthews; Eyal Feigenbaum**

Physical and Life Sciences and National Ignition Facility and Photon Sciences, Lawrence Livermore National Laboratory, Livermore, CA, 94550

KEYWORDS dewetting, solid-state diffusion, thermal annealing, gold nanoparticle, large-scale plasmonic array, tunable nanoparticle ensemble

ABSTRACT Gold nanoparticles are important constituents in plasmonic arrays, lending themselves to electronic, optical, biomedical, sensing, and catalytic applications, among numerous others. Process variables that must be controlled when engineering plasmonic nanoparticle ensembles include nanoparticle size, shape, and spatial distribution on surfaces. The challenge in generating arrays of nanoparticles with control over these three parameters increases dramatically as spatial requirements for uniformity extend to larger processing areas. We present a procedure that exploits thermally driven solid-state diffusional dewetting to yield considerable flexibility in generating ensembles of gold nanoparticles. Such sub-melting dewetting introduces fine control over particle spatial features that are currently difficult to achieve through conventional methods of generating nanoparticle arrays. Due to the simplicity of the process and its area-scalability, solid-state diffusional dewetting is shown here to be a method that could be easily scaled up to apply to large-area plasmonic fabrication processes.

Introduction

Plasmonic applications, governed by enhanced light-matter interactions that are reshaped by the interaction of light with nanoscale metallic structures, have garnered extensive interest in recent years. The local plasmonic resonances supported by metal nanoparticles result in an electromagnetic field intensification, leading to a locally-enhanced interaction with matter on a sub-diffraction-limited volume. Metal nanoparticles enhance the coupling between the near-field and the far-field, for potential usage of guiding more light into and out from a specific small interaction volume [1] [2] [3]. These properties result in increasingly growing plasmonic-enhanced applications for metal nanoparticle arrays, e.g., sensing [4], photovoltaics [5], photocatalysis [6], and displays [7]. There are many aspects of control that must be considered when engineering plasmonic nanoparticle arrays, such as the nanoparticle (NP) size, shape, and spatial distribution; these arise as a result of the sensitivity of the local plasmonic resonance to the details of the individual NP, as well as the space between neighboring particles [8] [3].

While there are many plasmonic NP systems, gold is of particular interest as it is inert and has a plasma frequency below the visible range, and thus the plasmonic resonance can be tuned (with relatively low attenuation) across the visible and near-infrared regions through regulation of the NP shape, size, and interparticle spacing. Gold is prevalent among surface-enhanced Raman spectroscopy (SERS) applications, where enhancement factors attributed to gold nanospheres have been found to increase up to 10^9 for the appropriate Au nanosphere size and separation distance [4]. Other advances of gold as a plasmonic material include nanofocusing with accompanying optical nonlinearities [9], photothermal therapy through thermoplasmonics [10], and photocatalysis [11]. The appeal, and the challenge, of this technology is that the plasmonic absorption depends strongly on the shape and size of the NP, and may be modified through close

packing of NP via interparticle coupling (e.g., formation of dimers) [2]. Therefore, the ability to tailor these parameters of plasmonic NP arrays will enable application-specific optimization of particle ensembles. The beneficiaries of *controllable large-scale plasmonic arrays* are embedded within many interdisciplinary fields, including enhanced photovoltaics [5], sensing and detection of biomolecules [12] [13], catalysis [14] [15], optical filters [1], displays [7], and numerous others. A persisting challenge that needs to be overcome when attempting to design plasmonic NP ensembles is the ability to control these spatial features on a large scale.

Current approaches to generating large-scale gold NP ensembles include bottom-up techniques such as citrate stabilization of nanocrystalline Au growth [16], in which the plasmonic properties can be adjusted by controlling parameters affecting self-assembly. Seeded Au growth techniques are inherently wet bench methods, so care must be implemented to remove all precursor materials to avoid unwanted absorption/contamination sites at the final NP ensemble. Additional techniques include spin-coating and dip-coating, although utilization of spin- and dip-coating may introduce uncertainty into the uniformity of the NP array, both through particle spacing inhomogeneity as well as NP distribution potentially manifesting itself as a NP size gradient within the ensemble.

An alternative method to generate NP arrays that avoids both the inclusion of additional materials as well as spatial uniformity issues within the NP array is dewetting – an easy and simple process employed to produce randomly oriented NP ensembles on a substrate. Spinodal dewetting, the consequence of ultra-fast heating beyond the material's melting temperature, occurs when thin liquified films assemble into droplets as surface tension stability is overcome by attractive intermolecular forces. To date, extensive investigations into spinodal dewetting of thin Au films to fabricate NP ensembles have been conducted [17] [18] [19]. Through spinodal dewetting, a stochastic self-assembly process occurs in which the resultant mean particle diameter, *D*, and

nearest neighbor spacing, Λ, are determined by the initial film thickness, *h*. The nearest neighbor center-to-center distance (henceforth referred to as period) follows the relationship [19]

$$\Lambda = \sqrt{\frac{16\,\pi^3\gamma}{A}}\,h^2 \tag{1}$$

for spinodal dewetting, where γ is the surface tension of the liquid film and A is the Hamaker coefficient. In the case of Au/SiO_2 composite systems, work reported by Kalyanaraman et al. [19] found the NP period satisfied a power law according to

$$\Lambda = 2.43 \cdot h^2 \tag{2}$$

with particle diameter

$$D = 1.83 \cdot h^{5/3} \tag{3}$$

The restriction when using spinodal dewetting is this exclusive determination of the particle size and spacing by the initial film thickness [19]. A composite system with a given initial film thickness will constrain the NP size and spacing between adjacent particles, with limited ability to adjust spacing (size) while holding size (spacing) constant. To control NP size or period through spinodal dewetting, an adjustment to the period or diameter on the order of a few tens of nanometers requires modification of the initial film thickness at the Å scale.

To overcome this challenge we rely on thermally driven solid-state diffusional dewetting to generate ensembles of plasmonic gold NPs with flexibility in independently adjusting NP size, spacing, and shape that is difficult to achieve by traditional approaches to spinodal dewetting. Previous studies probing solid-state thermal dewetting of Au films on glass monitored the time evolution of Au NP at a constant annealing temperature [20]. Here, we map out the parameter space of the generated plasmonic NP ensembles as a function of the annealing temperature while investigating Au films of thicknesses that generate fundamentally different morphologies of Au on the fused silica substrates. Due to the simplicity of the process and its area-scalability, solid-

state diffusional dewetting can be easily applied to large-area plasmonic applications. Furthermore, this process can be adapted to suit different plasmonic NP/substrate systems through processing parameter alterations.

Experimental

In addition to its plasmonic properties, gold was selected for this study due to its surface tension and high Hamaker coefficient (and subsequently small predicted NP size), as well as its resistance to oxidation; fused silica (FS) was chosen as the substrate material due to its abundance in optical applications and high glass transition temperature. Thin gold films deposited on FS were annealed at different temperatures with a temperature increase of about 20 °C·min^{-1}, after which the furnace temperature was held at the set temperature for 30 min. Auxiliary studies into the temperature reached on the substrate surface were conducted, see supplemental material. All temperatures reported here are the maximum temperature of the substrate. Due to the slow heating ramp, solid state dewetting initiates as the Au film temperature increases but is still well below the bulk melting temperature of gold (1064 °C), with the NP experiencing size-dependent melting for the highest temperature studied. Illustration of sample fabrication is depicted in Figure 1(a), with deposition of Au film (sample-dependent Au thickness) in step ii, and the generation of the NP ensemble through annealing in step iii. Figure 1(b) – (i) display electron micrographs taken from initial Au film thicknesses and annealing temperatures according to: (b) – (c) 5 nm Au film annealed at 860 °C and 1010 °C, respectively, (d) – (e) 7.5 nm Au annealed at 320 °C and 1060 °C, respectively, (f) – (g) 10 nm Au annealed at 320 °C and 860 °C, respectively, and (h) – (i) 12.5 nm Au annealed at 540 °C and 1060 °C, respectively. The upper right insets in Figure 1(b) – (i) display the respective samples in reflectance mode to visually illustrate the change in their optical properties introduced by modifying the plasmonic resonance. The lower left insets

depict magnified portions of the SEM images to assist in resolving small features. Inspection of the SEM images in Figure 1 illustrates that, for a given initial film thickness, the annealing temperature impacts the NP size, separation distance between particles, and the ellipticity of the NP ensemble.

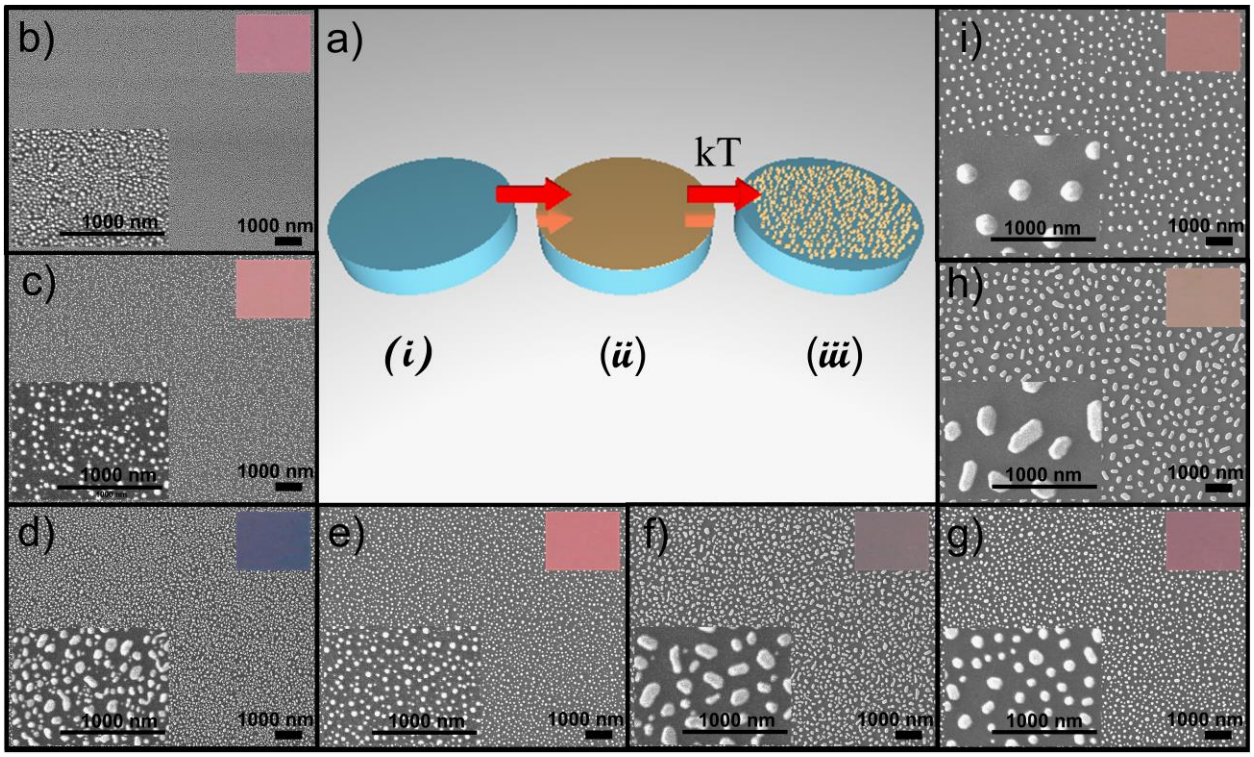

Figure 1. Panel (a): sample fabrication consisting of deposition of thin Au film onto fused silica substrate (step ii), after which the film is heated to generate the NP ensembles (step iii). Panels (b) – (i) correspond to NP ensembles generated from different sample and processing parameters, discusssed in details in the text. All SEM scale bars are 1 μm, and upper right insets are images taken in reflectance mode.

Results and Discussion

To generate NP arrays on surfaces with sizes and separation distances producing plasmonic resonance in the visible range, as evident from the color changes in Figure 1 insets, the target thicknesses of the thin Au films were carefully chosen to be near the transition value at which the deposited Au creates a continuous film across the fused silica interface, otherwise known as the percolation limit. Film thicknesses below the percolation limit produce isolated nanoislands upon deposition, while films significantly above this threshold generate continuous (planar) Au films [20]. For the work reported here, four target film thicknesses were investigated: 5 nm, 7.5 nm, 10 nm, and 12.5 nm Au; Figure 2 displays the film morphologies for those four thicknesses in panels (a) – (d), respectively. In each panel there are two SEM images – the left micrograph depicts the as-deposited Au morphology, and the right image presents the plasmonic NP array following annealing at 650 °C. The scale bars for all as-deposited images are 500 nm, while those of the NP arrays are 1 μm. Referring to the as-deposited images, it is observed that the 7.5 nm – 12.5 nm Au films have varying void densities shown as the darker regions of the images. As the target thickness decreases from 12.5 nm in Figure 2(d) to 7.5 nm in Figure 2(b), the in-plane electrical conductivity decreases by a factor of 25 as the film becomes more disconnected with the presence of these void spaces. Continuing this trend, the 5 nm film falls below the percolation limit as illustrated by the morphology transitioning from semi-contiguous in the cases of thicker films to non-contiguous – i.e. electrically discontinuous islands. We note that the morphology of the initial film (transitioning from electrically continuous to non-contiguous) is paramount to the generation of the final dewet structure, as low temperature processing is governed by solid state diffusion and the degree of gold interconnectedness is significant. Consequently, the fraction of void space in the as-deposited morphology constrains the topography of the final plasmonic ensemble. Evidence of this is illustrated in Figure 2, where the final dewetting structures of the four films are shown following

a 30 min anneal at 650 °C. At this temperature, substantially below Au bulk melting T_m = 1064 °C, solid state diffusional dewetting (SSD) is unequivocally the mechanism at play. What was unclear, however, was the extent to which the process is controlled through the annealing temperature and whether the steady-state NP configuration can be manipulated by processing parameters and the initial film morphology to yield different NP sizes.

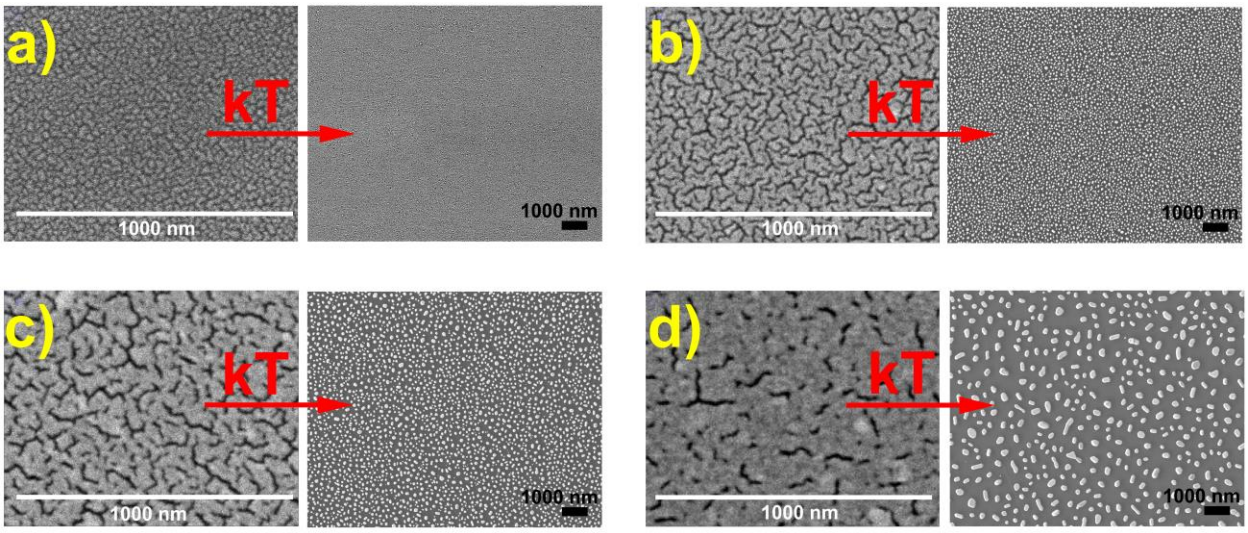

Figure 2. Scanning electron micrographs displaying Au (light color) on FS substrates (dark color) in the as-deposited state (left) and following SSD at 650 °C (right) with the following initial Au thicknesses: (a) 5 nm, (b) 7.5 nm, (c) 10 nm, and (d) 12.5 nm.

To probe the correlation between as-deposited morphology and final NP topography, a temperature-dependency study of shape, size, and spacing was explored for 5, 7.5, 10, and 12.5 nm Au film thicknesses, all of which are near the percolation limit. In this region of close proximity to the percolation limit, a small change in film thickness produces a significant change in the film morphology. Through SEM analysis, contour plots of the NP ensemble mean major axis, period,

and aspect ratio obtained via SSD are displayed in Figure 3 as functions of initial film thickness and annealing temperature. To further relate the plasmonic behavior to the spatial features of the nanoparticles, resultant nanoparticle size distributions, including the mean minor axis dimensions, are reported in the supplemental work for all annealing conditions investigated. Gold nanospheres do not experience a significant melting point depression until the diameter is reduced to roughly 40 nm [21] [22]. In this work, the melting point depression of the NP ensembles depicted in Figure 3 did not result in melting of the mean NP size until the highest T = 1060 °C anneal, emphasizing the extent to which solid-state diffusion is driving this process.

As is evident from Figure 3 (a) – (b), both the mean particle size and period can be determined by the annealing temperature. As general trends, it is observed that with increasing film thickness at a given temperature, both the particle size and period increase. The same generalizations cannot be made for the size or period at a constant film thickness. For a given film thickness, how size and period evolve with an increase in temperature depend on the initial film thickness itself. To illustrate this point, the period of the NP array from a 5 nm film increases with increasing temperature, while the period of a 12.5 nm film decreases with increasing temperature. Figure 3(a) – (b) reveal the existence of different behavioral zones in this parameter space, namely NP ensembles generated from films that are initially non-contiguous versus those that are electrically contiguous.

On the other hand, the aspect ratio seen in Figure 3(c) exhibits the same tendency for all film thicknesses – increasing annealing temperature drives the particles more circular (their areal projection onto the substrate). This finding is justified due to the higher mobility in the system with elevating temperature, culminating in melting of the mean NP size for the 1060 °C anneal.

The contact angle for gold on fused silica is 143° at 1353 K [23], signaling the tendency for gold to self-agglomerate to optimize the interfaces between Au, FS, and the ambient environment.

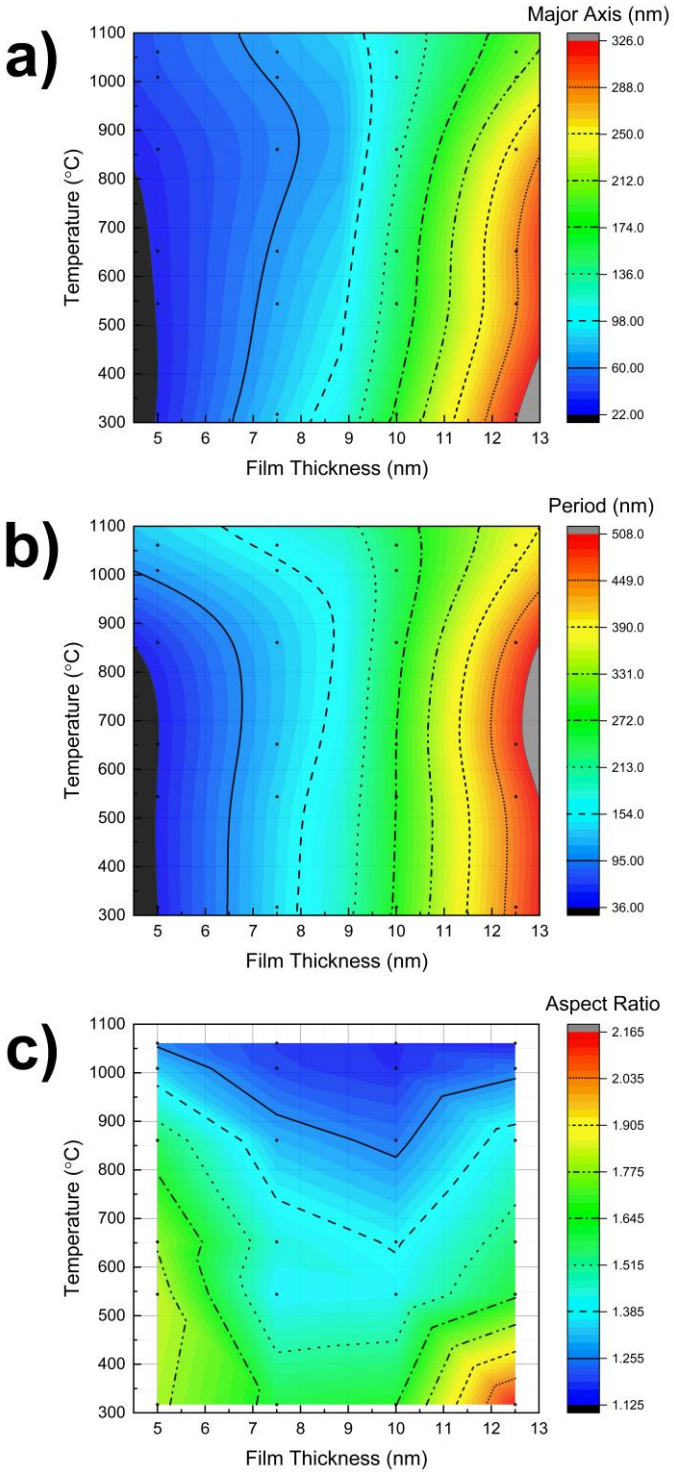

Figure 3. Contour plots of (a) mean major axis length, (b) center-to-center distance (period), and (c) aspect ratio of generated NP ensemble as functions of annealing temperature and initial film thickness. Note: the colors of the contour plots do not correspond to the same scales.

As highlighted by Figure 3(c), there is a temperature-dependent degree of ellipticity controllable through this process revealed by the aspect ratio under steady-state conditions. Recall that the thermal processing consists of a 30 min anneal at the set temperature. To assess the degree to which steady-state conditions have been met, separate experiments were conducted in which the annealing time was expanded – see supplemental information. Our results agree with investigations by others [20] that steady-state has been reached before the conclusion of a 30 min anneal, even for the lowest temperatures. This indicates that there is a *steady-state elliptical shape* of the particles as a function of temperature that causes ellipticity without any apparent axis of symmetry. The as-deposited Au films are polycrystalline, but following the formation of isolated Au 'islands' (through diffusion) grain growth within the formed islands drives them toward single crystalline with increasing temperature [20]. This grain growth may introduce the temperature dependence of ellipticity as grain boundaries present barriers to grain growth being driven by the thermal anneal [24]. The asymmetry induced by this process is likely a result of the interplay between the as-deposited film morphology, grain boundaries, and ensuing grain boundary grooving in the early stages of SSD.

Examination of Figure 3 reveals a fundamental dynamic related to the film thickness increase, indicative of the transition from noncontiguous to electrically conductive morphology. Recall that h = 5 nm corresponds to noncontiguous films (as-deposited state consisting of isolated nanoislands), while thicker films have varying degrees of areal void density within the respective film, refer back to Figure 2. The tendency for thick films (10 and 12.5 nm Au) to dewet as particles that get smaller with increasing annealing temperature is apparent in Figure 3(a). The noncontiguous film, however, exhibited the opposite characteristic that an increase in temperature caused the particle dimensions to *increase*. Given the as-deposited nanoisland morphology, the

separation distance likely provides enough of a barrier at low T to prevent particle agglomeration, while at elevated temperatures the increased diffusivity enables Ostwald ripening and growth of the particles. The intermediate role is exhibited by the 7.5 nm film, where for T < 900 °C the particles decrease in size through annealing, while temperatures greater than ~900 °C provide enough thermal energy to the system to overcome the separation distance between adjacent NP. Comparison of all three panels in Figure 3 shows that in each case, there is a shift in behavior as the film thickness approaches ~9 nm, suggesting this is the target thickness at which a critical coverage is met as the as-deposited films transition from noncontiguous nanoislands to an electrically continuous and conductive morphology.

Likewise it is seen in Figure 3(b) that the period may also be adjusted through control over annealing temperature, thus revealing the precision accessed through this process. For initial film morphologies either noncontiguous or approaching noncontiguity (in this study, the 5 nm and 7.5 nm Au films), the period begins to increase as the temperature approaches bulk melting. For the 12.5 nm Au film the reverse happens: the period decreases as the temperature approaches T_m. Both phenomena – the period increase that accompanies particle growth (increasing in height relative to the FS substrate) from thin initial films, as well as the division of large particles via enhanced mobility at elevated temperature which reduces the period – may be explained by increased diffusivity. These changes in period with annealing temperature represent an exciting possibility: through proper selection of initial film thickness and processing temperature, *particle size and interparticle spacing may be decoupled* to a large extent. Moreover, Figure 3 emphasizes the extent of control over the particle size, shape and spacing available through this process. In the

case of the 12.5 nm Au film, the particle major axis, period, and aspect ratio vary by 44%, 25%, and 48%, respectively, over the temperature range studied.

At annealing temperatures below the melting point of gold (adjusted for melting point depression of nanofeatures), solid state diffusion is the driving mechanism behind the gold coalescence into particles. However, for temperatures in excess of the melting temperature the mechanisims are still in question. Investigation into the length of time prior to steady-state acquisition, reported by Vaskevich et al. [20], found that the time necessary to satisfy steady-state conditions is on the order of 2 – 5 min at 550 °C. This indicates the heating rate of ~20 °C·min^{-1} implemented here is slow enough that the film-to-particle transition is likely near steady-state configuration. Therefore, the dewet structure is predefined by the SSD that precedes melting, even when T = 1060 °C. As expected, the NP mean size and period differ from the predictions by Eqns. (2) – (3) even for $T > T_m$, as those equations were derived from continuous liquid film considerations. The SSD data from Figure 3 is plot in Figure 4 against the predictions from Eqns. (2) – (3), where the range of the solid-state diffusional dewetting is indicated by the triangles. Comparison of the SSD results to those reported in literature [19], see Figure 4, confirm that spinodal dewetting criterion are not satisfied for $T > T_m$. In effect, the topography is 'locked-in' before the melting temperature is ever reached, giving rise to a NP ensemble microstructural evolution that remains distinct from spinodal dewetting. Figure 4 illustrates the strength of SSD:

making necessary adjustments to the annealing temperature enables a range of NP sizes and periods from a single initial film thickness that are unobtainable through spinodal dewetting.

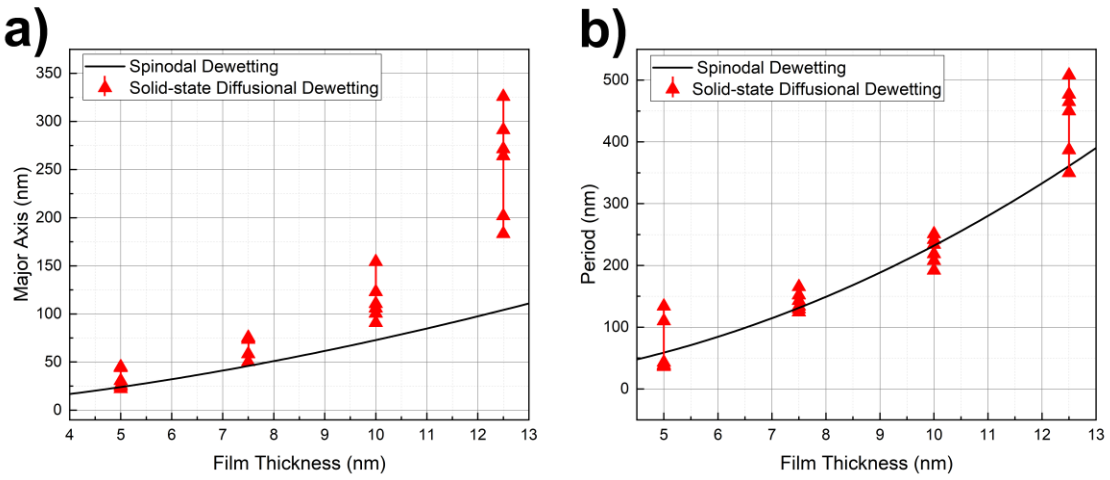

Figure 4. Comparison of spinodal dewetting predictions *[19]* to SSD values reported here for (a) particle major axis length, and (b) NP period. The solid-state diffusional dewetting data (red triangles) generated from Figure 3 illustrate the range of control available through SSD.

The modification of NP shape, size, and spacing achieved through SSD can be observed upon visual inspection of the NP ensemble due to the plasmonic resonance, and the resultant transmission spectra are shown in Figure 5. For all NP arrays investigated, data was collected at three different locations within the sample (irradiated area of 4 mm^2). The p-polarization transmission spectra depicted in Figure 5 are the mean transmission across the 3 locations, with the standard deviation incorporated as error bars. The top panel shows the transmission of NP generated via an initial film thickness of 5 nm, while the panels below it depict transmission of NP ensembles originating from 7.5, 10, and 12.5 nm film thicknesses.

For the NP array from the h = 5 nm film, the transmission minima shifts toward lower wavelengths as the temperature increases. NP transmission from the three thicker films follow the same trend found with the 5 nm film, i.e. extinction spectra blue-shifting with increasing temperature. Consequently, only the high temperature and low temperature spectra are necessary to identify the available plasmonic resonance range from each initial film thickness. The plasmon resonance shift is driven by the transition of the particles from a steady-state elliptical configuration (average aspect ratio of 1.8 across the four film thicknesses at the low temperature anneal) to a more hemispherical geometry with aspect ratio closer to unity for the highest processing temperature probed.

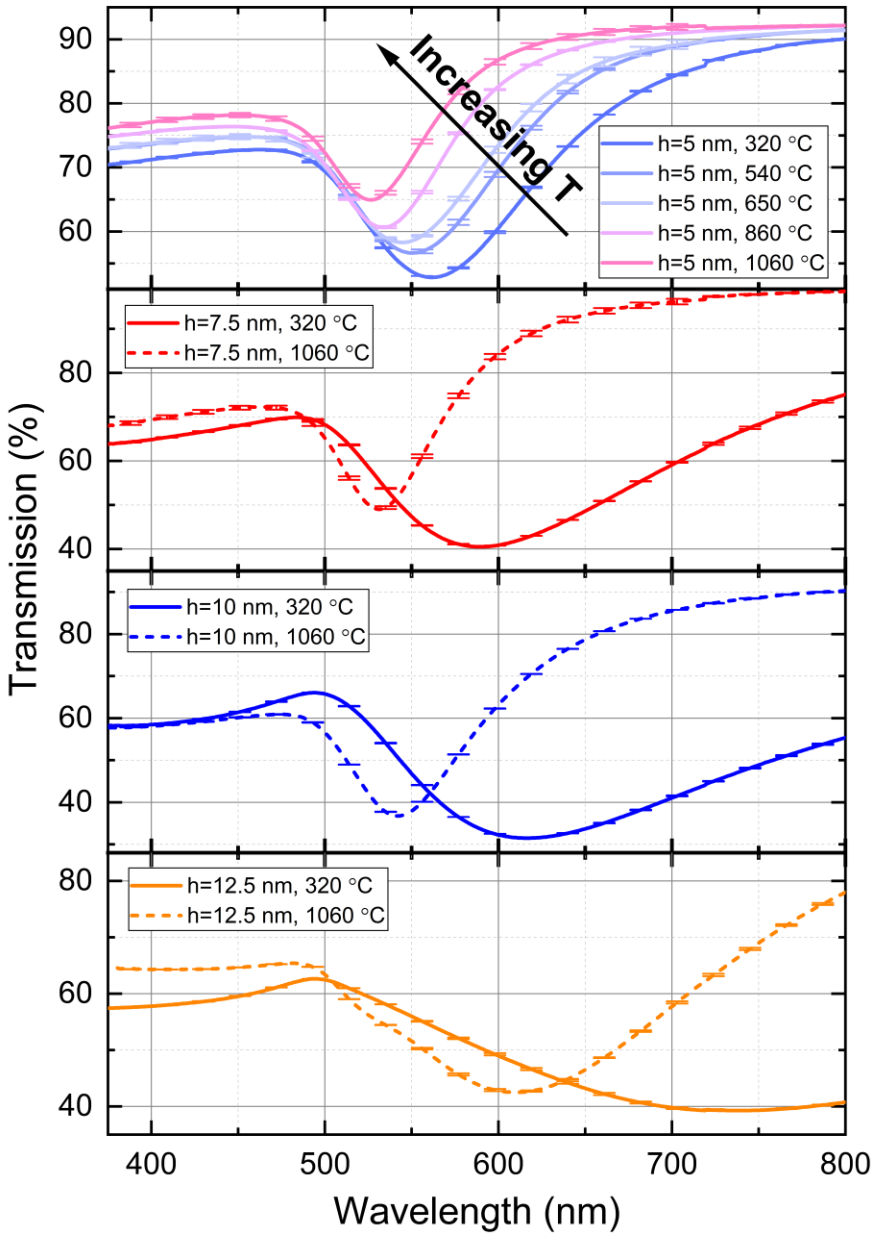

Figure 5. Transmission spectra of plasmonic NP ensembles generated through SSD; the panels are segregated by initial film thickness. For initial film thickness h = 5 nm (top panel), transmission profiles from all temperatures are shown. For the remaining three panels, the spectra generated from the lowest and highest temperatures are given to depict the plasmonic resonance range obtainable for the relevant thickness.

Closer inspection of the standard deviations found in Figure 5 gives insight into the degree of homogeneity associated with SSD. Even though the SSD process is random, it follows a stochastic distribution that, as evident from Figure 1 insets and Figure 5, varies insignificantly in space with respect to the intended resonance peak modifications. When the array is probed by light, the locally homogenized interaction of the light with the NP ensemble result is a small standard deviation: for the data presented in Figure 5, the largest value of standard deviation was 0.63%, whereas the resonance increases by 40% from the h = 5 nm array to the h = 12.5 nm array. This signifies that once length scales are sufficiently long, i.e. on the order of the optical properties resulting from an average over multi-wavelengths, the interaction of the light with the NP ensemble has very little spatial dependence. Thus, for large-scale applications the plasmon resonance variance induced by potential spatial nonuniformities is not a concern.

Conclusion

Au nanoparticles can be manipulated to yield ensembles with spatial features designed to satisfy application-specific requirements. The parameter space pertaining to generation of gold nanoparticle arrays on fused silica substrates has been dramatically increased in a process that is simple and scalable, expanding the possibilities for large-area plasmonic applications. Through solid state diffusional dewetting in a regime near the percolation limit of Au on fused silica, nanoparticle size, shape, and period can be controlled to facilitate engineered meter-scaled plasmonic nanoparticle arrays. Significantly, nanoparticle size and center-to-center period may be controlled *independently* – an ability that is inaccessible through spinodal dewetting. The ability to generate these NP ensembles will prompt immediate growth across many scientific disciplines, including, but not limited to, seeds for nanoparticle/rod growth, enhanced photovoltaics, displays, molecular detection, optical filters, and catalysis.

ASSOCIATED CONTENT

Supporting Information.

The following files are available free of charge:

Annealing recipes (PDF)

Nanoparticle size distributions at all annealing conditions (PDF)

Assessment of steady-state morphology acquisition (PDF)

In situ TEM analysis (PDF)

AUTHOR INFORMATION

Corresponding Author

*E-mail: feigenbaum1@llnl.gov

Author Contributions

The manuscript was written through contributions of all authors. All authors have given approval to the final version of the manuscript.

ACKNOWLEDGMENT

This work was performed under the auspices of the U.S. Department of Energy by Lawrence Livermore National Laboratory under Contract DE-AC52-07NA27344 within the Laboratory Directed Research and Development Program (LDRD) at LLNL. (#18-ERD-005). LLNL-JRNL-771023

References

[1] Ozbay, Ekmel, "Plasmonics: Merging Photonics and Electronics at Nanoscale Dimensions," *Science,* vol. 311, no. 5758, pp. 189-193, 2006.

[2] Jiang, Nina; Zhuo, Xiaolu; Wang, Jianfang, "Active Plasmonics: Principles, Structures, and Applications," *Chemical Reviews,* vol. 118, p. 3054−3099, 2018.

[3] Stockman, Mark I., "Nanoplasmonics: past, present, and glimpse into future," *Optics Express,* vol. 19, no. 22, pp. 22029 - 22106, 2011.

[4] Ding, Song-Yuan; Yi, Jun; Li, Jian-Feng; Ren, Bin; Wu, De-Yin; Panneerselvam, Rajapandiyan; Tian, Zhong-Qun, "Nanostructure-based Plasmon-enhanced Raman Spectroscopy for Surface Analysis of Materials," *Nature Reviews Materials,* pp. 1-16, 2016.

[5] Atwater, Harry A.; Polman, Albert, "Plasmonics for Improved Photovoltaic Devices," *Nature Materials,* vol. 9, pp. 205-213, 2010.

[6] Zhou, Linan; Zhang, Chao; McClain, Michael J.; Manjavaca, Alejandro; Krauter, Caroline M.; Tian, Shu; Berg, Felix; Everitt, Henry O.; Carter, Emily A.; Nordlander, Peter; Halas, Naomi J., "Aluminum Nanocrystals as a Plasmonic Photocatalyst for Hydrogen Dissociation," *Nano Letters,* vol. 16, pp. 1478-1484, 2016.

[7] Xu, Ting; Wu, Yi-Kuei; Luo, Xiangang; Guo, L. Jay, "Plasmonic Nanoresonators for High-Resolution Colour Filtering and Spectral Imaging," *Nature Communications,* pp. 1-5, 2010.

[8] Dong, Liangliang; Yang, Xiao; Zhang, Chao; Cerjan, Benjamin; Zhou, Linan; Tseng, Ming L.; Zhang, Yu; Alabastri, Alessandro; Nordlander, Peter; Halas, Naomi J., "Nanogapped Au Antennas for Ultrasensitive Surface-Enhanced Infrared Absorption Spectroscopy," *Nano Letters,* vol. 17, pp. 5768-5774, 2017.

[9] Schmidt, Slawa; Piglosiewicz, Bjorn; Sadiq, Diyar; Shirdel, Javid; Lee, Jae S.; Vasa, Parinda; Park, Namkyoo; Kim, Dai-Sik; Lienau, Christoph, "Adiabatic Nanofocusing on Ultrasmooth Single-Crystalline Gold Tapers Creates a 10-nm-Sized Light Source with Few-Cycle Time Resolution," *ACS Nano,* vol. 6, no. 7, pp. 6040-6048, 2012.

[10] Gobin, Andre M.; Lee, Min Ho; Halas, Naomi J.; James, William D.; Drezek, Rebekah A.; West, Jennifer L., "Near-Infrared Resonant Nanoshells for Combined Optical Imaging and Photothermal Cancer Therapy," *Nano Letters,* vol. 7, no. 7, pp. 1929-1934, 2007.

[11] Clavero, César, "Plasmon-induced hot-electron generation at nanoparticle/metal-oxide interfaces for photovoltaic and photocatalytic devices," *Nature Photonics,* vol. 8, pp. 95-103, 2014.

[12] Aslan, Kadir; Lakowicz, Joseph R.; Geddes, Chris D., "Metal-Enhanced Fluorescence Using Anisotropic Silver Nanostructures: Critical Progress to Date," *Analytical Bioanalytical Chemistry,* no. 382, p. 926–933, 2005.

[13] Lakowicz, Joseph R., "Plasmonics in Biology and Plasmon-Controlled Fluorescence," *Plasmonics,* vol. 1, p. 5–33, 2006.

[14] Christopher, Phillip; Xin, Hongliang; Linic, Suljo, "Visible-light-enhanced catalytic oxidation reactions on plasmonic silver nanostructures," *Nature Chemistry,* vol. 3, p. 467–472, 2011.

[15] Huang, Xiaoqing; Tang, Shaoheng; Mu, Xiaoliang; Dai, Yan; Chen, Guangxu; Zhou, Zhiyou; Ruan, Fangxiong; Yang, Zhilin; Zheng, Nanfeng, "Freestanding Palladium Nanosheets with Plasmonic and Catalytic Properties," *Nature Nanotechnology,* vol. 6, p. 28–32, 2011.

[16] Cheng, Wenlong; Dong, Shaojun; and Wang, Erkang , "Two- and Three-Dimensional Au Nanoparticle/CoTMPyP Self-Assembled Nanotructured Materials: Film Structure, Tunable Electrocatalytic Activity, and Plasmonic Properties," *Journal of Physical Chemistry B,* vol. 108, pp. 19146-19154, 2004.

[17] Bischof, J.; Scherer, D.; Herminghaus, S.; Leiderer, P., "Dewetting Modes of Thin Metallic Films: Nucleation of Holes and Spinodal Dewetting," *The American Physical Society,* vol. 77, no. 8, 1996.

[18] Herminghaus, Stephan; Jacobs, Karin; Mecke, Klaus; Bischof, Jorg; Fery, Andreas; Ibn-Elhaj, Mohammed; Schlagowski, Stefan, "Spinodal Dewetting in Liquid Crystal and Liquid Metal Films," *Science,* vol. 282, pp. 916-919, 1998.

[19] Yadavali, Sagar; Khenner, Mikhail; Kalyanaraman, Ramki, "Pulsed Laser Dewetting of Au films: Experiments and Modeling of Nanoscale Behavior," *Journal of Material Research,* vol. 28, no. 13, pp. 1715-1723, 2013.

[20] Tesler, Alexander B.; Maoz, Ben M.; Feldman, Yishay; Vaskevich, Alexander; Rubinstein, Israel, "Solid-State Thermal Dewetting of Just-Percolated Gold Films Evaporated on Glass: Development of the Morphology and Optical Properties," *Journal of Physical Chemistry C,* vol. 117, p. 11337−11346, 2013.

[21] Buffat, Ph.; Borel, J-P., "Size effect on the melting temperature of gold particles," *Physical Review A,* vol. 13, no. 6, pp. 2287-2298, 1976.

[22] Schmid, Günter; Corain, Benedetto, "Nanoparticulated Gold: Syntheses, Structures, Electronics, and Reactivities," *Eur. J. Inorg. Chem.,* pp. 3081-3098, 2003.

[23] Sangiorgi, Roberto; Muolo, Maris L.; Chatain, Dominique; Eustathopoulos, Nicolas, "Wettability and Work of Adhesion of Nonreactive Liquid Metals," *Journal of American Ceramic Society,* vol. 71, no. 9, pp. 742-748, 1988.

[24] Jacquet, P.; Podor, Renaud; Ravaux, Johann; Lautru, J.; Teisseire, Jérémie; Gozhyk, Iryna; Jupille, Jacques; Lazzari, Rémi, "On the Solid-State Dewetting of Polycrystalline Thin Films: Capillary versus Grain Growth Approach," *Acta Materialia,* vol. 143, pp. 281-290, 2018.

[25] Castro, T.; Reifenberger, R.; Choi, E.; Andres, R. P., "Size-dependent melting temperature of individual nanometer-sized metallic clusters," *Physical Review B,* vol. 42, no. 13, pp. 8548 - 8556, 1990.

[26] Tesler, Alexander B.; Maoz, Ben M.; Feldman, Yishay; Vaskevich, Alexander; Rubinstein, Israel, "Solid-State Thermal Dewetting of Just-Percolated Gold Films Evaporated on Glass: Development of the Morphology and Optical Properties," *Journal of Physical Chemistry C,* vol. 117, p. 11337−11346, 2013.

Table of Contents (TOC) Graphic